DTU Library

Bilirubin oxidase oriented on novel type three-dimensional biocathodes with reduced graphene aggregation for biocathode

Tang, Jing; Yan, Xiaomei; Huang, Wei; Engelbrekt, Christian; Duus, Jens Øllgaard; Ulstrup, Jens; Xiao, Xinxin; Zhang, Jingdong

Bilirubin oxidase oriented on novel type three-dimensional biocathodes with reduced graphene aggregation for biocathode

Jing Tang[a], Xiaomei Yan[a], Wei Huang[a], Christian Engelbrekt[a], Jens Øllgaard Duus[a], Jens Ulstrup[a,b], Xinxin Xiao[a,*], Jingdong Zhang[a,*]

[a] Department of Chemistry, Technical University of Denmark, Kongens Lyngby 2800, Denmark

[b] Kazan National Research Technological University, K. Marx Str., 68, 420015 Kazan, Republic of Tatarstan, Russian Federation

* Corresponding Authors: xixiao@kemi.dtu.dk (X. Xiao) and jz@kemi.dtu.dk (J. Zhang)

Abstract: Aggregation of reduced graphene oxide (RGO) due to π-π stacking is a recurrent problem in graphene-based electrochemistry, decreasing the effective working area and therefore the performance. Dispersing RGO on three-dimensional (3D) carbon paper electrode is one strategy towards overcoming this, which partially relieves aggregation. In this report, we describe the graft of negatively charged 4-aminobenzoic acid (4-ABA) onto a graphene functionalized carbon paper electrode surface. 4-ABA functionalization induces separation of the RGO layers, at the same time leading to favorable orientation of the blue multi-copper enzyme *Myrothecium verrucaria* bilirubin oxidase (*Mv*BOD) for direct electron transfer (DET) in the dioxygen reduction reaction (ORR) at neutral pH. Simultaneous electroreduction of graphene oxide to RGO and covalent attachment of 4-ABA are achieved by applying alternating cathodic and anodic electrochemical potential pulses, leading to a very high catalytic current density (Δj_{cat}:193 ± 4 μA cm^{-2}) under static conditions. Electrochemically grafted 4-ABA not only leads to a favorable orientation of BOD as validated by fitting a kinetic model to the electrocatalytic data, but also acts to alleviate RGO aggregation as disclosed by scanning electron microscopy, most likely due to the electrostatic repulsion between 4-ABA-grafted graphene layers. With a half-lifetime of 55 h, the bioelectrode also shows the highest operational stability for DET-type *Mv*BOD-based bioelectrodes reported to date. The bioelectrode was finally shown to work well as a biocathode of a membrane-less glucose/O$_2$ enzymatic biofuel cell with a maximum power density of 22 μW cm^{-2} and an open circuit voltage of 0.51 V.

Keywords: Reduced graphene oxide; bilirubin oxidase; carbon paper; 4-aminobenzoic acid monolayer; direct electron transfer; gas diffusion bioelectrode.

1. Introduction

Highly efficient and stable enzymatic bioelectrodes are key in the development of sustainable electrochemical bio-devices such as enzymatic biofuel cells (EBFCs), which presently attract increasing attention (Li et al., 2020; Ruff et al., 2018; Wang et al., 2020; Xiao et al., 2020; Xiao et al., 2019). The implementation of conductive nanomaterials for electrode modification offers here great promise (Le et al., 2016; Xiao et al., 2017; Xiao et al., 2019). Nanomaterials with high specific surface area improve enzyme loading, but are often accompanied by substrate diffusion limitations (Xiao et al., 2018; Zhao et al., 2017). Three-dimensional (3D) porous nanomaterials, with an open structure, simultaneously can alleviate limitations as to substrate supply and offer new possibilities for controlling enzyme orientation at the surface to facilitate direct electron transfer (DET) (Siepenkoetter et al., 2016; Xiao et al., 2018). In addition, 3D structures offer significant advantages through enzyme confinement, which ensures both efficient electronic coupling to the working electrodes (Siepenkoetter et al., 2017) and high enzyme stability (Mano and de Poulpiquet, 2018; Murata et al., 2009; Xiao et al., 2019).

Given its remarkable mechanical flexibility, favorable electronic properties, and light mass, graphene has recently been intensely studied as electrode support for bioelectrocatalysts for sensing or wearable bioelectronics applications (Pavlidis et al., 2014; Yu et al., 2019). However, pristine graphene itself, typically produced by mechanical exfoliation or chemical vapor deposition, has not been widely explored as bioelectrode material most likely due to the absence of functional surface groups such as carboxylic acid and amino groups suitable for enzyme immobilization (Wei et al., 2020). Reduced graphene oxide (RGO) is a better candidate for enzyme support due to the presence of residual oxygenated species on the basal planes and edges of the RGO sheets (Hernández-Cancel et al., 2015). RGO is usually produced chemically (Werchmeister et al., 2019), thermally (Dreyer et al., 2010) or electrochemically (Tang et al., 2019) based on an easy-to-handle

3

61 method. 3D graphene-based electrodes such as graphene papers (Shen et al., 2019a; Shen et al.,

62 2019b) and graphene modified 3D electrodes (Tang et al., 2019; Werchmeister et al., 2019) with

63 high surface area have emerged for enzymatic bioelectrodes with high catalytic current densities

64 (Qiu et al., 2017). However, aggregation of RGO sheets is a recurrent problem, resulting in loss of

65 active surface area (Dreyer et al., 2010). One strategy to relieve aggregation is to combine graphene

66 with "spacers" such as carbon nanotubes (CNTs), polymers or silica particles (Lawal, 2019; Li et

67 al., 2018; Yang et al., 2015). In our previous study (Tang et al., 2019), graphene oxide (GO) was

68 reduced electrochemically directly onto 3D carbon paper (CPs), which resulted in well-performing

69 bioelectrodes, but aggregation of RGO was not fully suppressed. Introducing hydrophilic surface

70 groups such as sulfonic acid groups can also increase the dispersibility and separation of graphene

71 layers in water (Zhao et al., 2011). Obtaining well-dispersed graphene free of aggregation while

72 maintaining high electrical conductivity is thus paramount for bioelectrochemical applications.

73 Bilirubin oxidase (BOD) and laccase belong to the family of multi-copper oxidases (MCOs), and

74 are known as efficient bioelectrocatalysts for the four-electron dioxygen reduction reaction (ORR)

75 at mild pH (Gross et al., 2017; Xia et al., 2016a). MCOs have been widely immobilized on solid

76 electrodes, serving as biocathodes for EBFC applications (Korani and Salimi, 2015; Mano and de

77 Poulpiquet, 2018; Murata et al., 2009). MCOs hold four copper atoms, of three types: Cu_{T1}, Cu_{T2}

78 and Cu_{T3} (Samejima et al., 1994). In ORR, Cu_{T1} receives electrons either from natural electron

79 donors or from solid electrode surfaces (*i.e.* DET). The electrons are subsequently transferred to

80 the trinuclear Cu_{T2}/Cu_{T3} center, where bound O_2 is reduced to H_2O (Al-Lolage et al., 2019; Gross

81 et al., 2017). The electrocatalytic performance of well-oriented MCO on a solid electrode surface

82 for dioxygen reduction is usually hampered by diffusion limitations and limited concentration of

83 dissolved O_2 (~1.2 mM maximum at neutral pH and 1 atm O_2) in aqueous solution (Mano and de

84 Poulpiquet, 2018). To circumvent this limitation, an air-breathing electrode, where O_2 would

4

85   diffuse directly from the air to the electrode, is practical (So et al., 2017). On the other hand, with

86   sufficient dioxygen supply, the rate of interfacial electron transfer between the electrode and the

87   Cu_{T1} site greatly affects the DET-electrocatalytic currents of MCO bioelectrode because the rate

88   decreases exponentially with increasing electron tunneling distance (Chi et al., 2005; Léger et al.,

89   2002; Mano and de Poulpiquet, 2018). Based on views on intramolecular electron transfer in

90   protein systems and quantum mechanical electron transfer concepts, efficient DET over more than

91   1.5 nm is not feasible (Chi et al., 2005; Gray and Winkler, 2010; Moser et al., 1992), highlighting

92   the importance of proper MCO orientation on the electrode for efficient electrocatalysis. Electrode

93   surface modification with substrate-mimicking molecules is an established approach to achieve

94   favorable MCO orientation on the electrode surface (Cracknell et al., 2011; Lopez et al., 2014;

95   Olejnik et al., 2012). The electrostatic and hydrophobic micro-environment around the Cu_{T1} site

96   is here crucial.

97   The most widely studied, *Myrothecium verrucaria* BOD (*Mv*BOD) undergoes efficient DET on

98   negatively charged surfaces (Lalaoui et al., 2015), while *Bacillus pumilus* BOD does so on

99   positively charged surfaces (Mazurenko et al., 2016). These studies highlight the importance of

100 understanding the specific enzyme at the molecular level and engineering of electrode surfaces at

101 the nanoscale. Another route is enzyme engineering introduced free cysteine residues which can

102 be specifically linked to electrode surfaces by covalent binding *via* maleimide groups (Al-Lolage

103 et al., 2019), enabling considerable DET of *Magnaporthae oryzae* BOD. Recently, high DET

104 bioelectrocatalytic current densities of BOD (up to ~0.2 mA cm^{-2} in static dioxygen-saturated

105 phosphate buffer solution, PBS) on electrochemically reduced GO electrodes modified with

106 negatively charged groups were achieved (Di Bari et al., 2016), but inevitable aggregation of the

107 ca. 200 μm GO flakes remained.

108   In order to overcome the problematic RGO aggregation, in the present study we have employed

109   3D CPs as supports for RGO modified with a negatively charged surface linker molecule 4-

110   aminobenzoic acid (4-ABA) to enable highly efficient DET of *Mv*BOD. As a novel approach, the

111   reduction of GO and grafting of 4-ABA were achieved simultaneously using electrochemical pulse

112   treatment with cathodic and anodic potentials applied alternatively. Scanning electron microscopy

113   (SEM) showed that RGO aggregation was in fact alleviated, implying that 4-ABA prevents π-π

114   stacking of RGO due to electrostatic repulsion. 4-ABA also plays an important role in proper

115   orientation of *Mv*BOD, validated both by high electrocatalytic current densities and by model

116   simulation of the electrocatalytic currents. The BOD bioelectrode exhibits furthermore a

117   surprisingly long half-life time of 55 h, to the best of our knowledge so far the best operational

118   stability reported for *Mv*BOD. The bioelectrodes were then exploited in a gas diffusion electrode

119   (GDE) configuration, registering elevated electrocatalytic current densities compared to the

120   immersed bioelectrodes. The *Mv*BOD GDE was further used as a biocathode in a glucose/O_2

121   EBFC, demonstrating their potential to harvest electricity from sugars.

122   2. Experimental

123   2.1 Chemicals and materials

124   2,2'-Azino-bis(3-ethylbenzothiazoline-6-sulfonic acid) diammonium salt (ABTS, ≥98%), D-(+)-

125   glucose (≥ 99%), potassium monohydrogen phosphate (K_2HPO_4, ≥ 99.999%) and potassium

126   dihydrogen phosphate (KH_2PO_4, ≥ 99.999%) were from Fluka (Germany), potassium

127   hexacyanoferrate(II) ($K_4[Fe(CN)_6]\cdot3H_2O$, 99.0-102.0%) and potassium permanganate ($KMnO_4$,

128   ≥99.9%) from Merck (Germany). Graphite powders (diameter < 20 μm), phosphorous pentoxide

129   (P_2O_5, ≥ 98%), potassium peroxodisulfate ($K_2S_2O_8$, ≥ 99%), sulfuric acid (H_2SO_4, 95-97%),

130   hydrogen peroxide (H_2O_2, 34.5-36.5%), hydrochloric acid (HCl, 37%), nitric acid (HNO_3, ≥ 65%),

131   hexaammineruthenium(III) chloride ($[Ru(NH_3)_6]Cl_3$, 98%), N-cyclohexyl-N'-(2-morpholinoethyl)

132 carbodiimide methyl-p-toluenesulfonate (CMC, 95%) and 4-ABA ($\geq$ 99%) from Sigma-Aldrich

133 (USA). *Mv*BOD (lyophilized powder, 15-65 unit mg^{-1} protein, molecular mass 60 kDa) and

134 glucose oxidase (GOD) (*Aspergillus niger*) (Type X+S. lyophilized powder, 100,000-250,000

135 units g^{-1} solid) were from Sigma-Aldrich (USA) and used as received. 190 μm-thick CP (product

136 No. EC-TP1-060) was from Quintech (Germany), 210 μm-thick hydrophobic CP (HCP, product

137 No. HCP120) and gas diffusion electrodes were from Shanghai Hesen Electric Co. Ltd (China).

138 Glue guns (Product no. PKP 18 E) with hot melt adhesive (i.e. polyvinyl chloride) from BOSCH

139 (Germany) were used to define a fixed geometric area of electrodes. 18.2 MΩ cm Millipore water

140 was used throughout.

141 **2.2 Fabrication of graphene-based bioelectrodes**

142 The synthesis of GO using a modified Hummer's method is described in our previous reports

143 (Seselj et al., 2018; Tang et al., 2019; Werchmeister et al., 2019). Prior to electrode modification,

144 the working surface area (0.50×0.50 cm^2) of T-shaped CP was defined with hot melt adhesive

145 using a glue gun, and coated with GO by sonication (denoted as CPG), Fig. S1 (Tang et al., 2019;

146 Werchmeister et al., 2019). Based on the measured water contact angle (WCA), cf. below the

147 resulting CPGs with different sonication duration were optimized to achieve surfaces of highest

148 possible hydrophilicity, Fig. S2. We fabricated BOD bioelectrodes (RGO-A/BOD), Scheme 1, on

149 the CPG substrates as follows: 20 μL GO suspension (3.0 mg mL^{-1}) was drop-cast onto a 0.25 cm^2

150 CPG electrode (labelled as CPG/GO electrode). After drying at room temperature (22 ± 2 °C), the

151 CPG/GO electrode with a loading of 0.24 mg cm^{-2} GO was reduced and functionalized

152 electrochemically by 15 cycles of alternating potential pulses at -1.4 V vs. Ag/AgCl (saturated

153 KCl) for 10 s and 1.4 V for 5 s in 15 mL Ar-saturated PBS (100 mM, pH 7.0) containing 5 mM 4-

154 ABA, resulting in the RGO-A electrode. The functionalized electrodes were washed with

155 Millipore water to remove loosely adsorbed 4-ABA. The activation of the –COOH groups was

7

156 achieved by incubating the RGO-A electrode in 5 mM CMC aqueous solution for 2 h at 4 °C.

157 Finally, 10 μL of 1.25 mg mL^{-1} BOD in 100 mM PBS (pH 7.0) was drop-cast onto the moist and

158 activated RGO-A electrode. The RGO-A/BOD electrodes were dried for 12 h, and then stored at

159 4 °C in a high-humidity atmosphere, *i.e.*, a 5.5 cm plastic Petri dish containing a wet tissue.

160 Control electrodes, including R-A/BOD without drop-cast GO suspension, RGO-A_ads/BOD

161 where BOD was physically adsorbed by omitting the CMC activation step, and RGO/BOD in the

162 absence of 4-ABA in PBS during electrochemical potential pulse treatment, were prepared

163 similarly. Bioelectrodes with -1.4/0 V pulses (narrow pulse, RGO-A(N)/BOD), and 0/1.4 V (GO-

164 A/BOD) where GO cannot be reduced, were prepared to investigate the role of potential pulse.
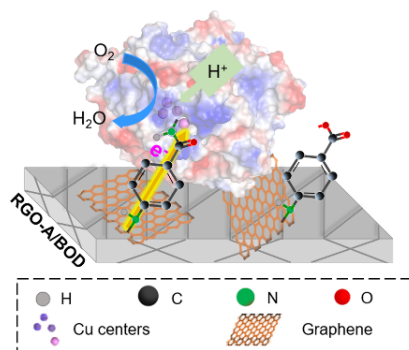
165
166
167 **Scheme 1.** Schematic illustration of the prepared RGO-A/BOD on a CPG electrode and its
168 bioelectrocatalytic process. A possible orientation of *Mv*BOD, with surface charge distribution
169 indicated by blue and red color symbolizing positive and negative charges, respectively, is shown
170 (not drawn to scale). The electrostatic representation is qualitatively determined based on charge-
171 smoothed potential from the PDB structure (2XXL) (Cracknell et al., 2011). The left 4-ABA linker
172 forms an amide bond with BOD, while the right 4-ABA with free –COO$^-$ remains unreacted.

173
174 **2.3 Characterization**

175 The morphology of functionalized electrodes was characterized by SEM (Quanta FEG 200, FEI,

176 USA) using an ETD detector. Atomic force microscopy (AFM) with a 5500 SPM system in

177 tapping mode (Keysight Technologies, USA) was chosen to probe the functionalized graphene

178 surface (*i.e.*, GO, RGO and RGO-A). X-ray photoelectron spectroscopy (XPS) of the modified

179 electrodes was recorded using an X-ray photoelectron spectrometer (ESCALABMKII, Thermo

180 Scientific, USA). The surface hydrophilicity was characterized using a contact angle system (OCA

181 Data Physics, Germany) to measure the WCA of dried electrodes with a droplet (6.0 µL) of

182 Millipore water on top.

183 **2.4 Electrochemical characterization**

184 The basic electrochemical behavior of graphene modified electrodes without BOD was

185 characterized by CV and electrochemical impedance spectroscopy (EIS) in 100 mM dioxygen-free

186 PBS (pH 7.0) containing 5.0 mM $K_4[Fe(CN)_6]$ or $[Ru(NH)_6]Cl_3$ using an Autolab PGSTAT12

187 system (Eco Chemie, Netherlands) with the NOVA 2.1 software. A three-electrode setup was

188 employed with graphene modified electrodes, a Pt wire, and Ag/AgCl (saturated) as the working,

189 counter, and reference electrodes, respectively. EIS was conducted at 0.24 V vs. Ag/AgCl, with

190 an applied amplitude of 10 mV in a frequency range 0.1 to 10^5 Hz. CV was recorded by scanning

191 the potential from 0 to 0.65 V at a scan rate of 50 mV s^{-1}. CV in blank PBS at 5 mV s^{-1} was used

192 to calculate the electrochemical surface area (ECSA).

193 CV, in the 0-0.65 V potential window at 5 mV s^{-1}, was used to characterize the ORR performance

194 of the BOD bioelectrodes. Prior to electrochemical measurements, RGO-A/BOD bioelectrodes

195 were immersed in 100 mM PBS (pH 7.0) for at least 30 min to remove loosely bound BOD

196 molecules. 15 mL 100 mM pH 7.0 PBS bubbled with either Ar or O_2 for 30 min was used as blank

197 electrolyte. The background-corrected ORR catalytic current density (Δj_{cat}), normalized to a

198 geometric area of 0.25 cm^2, was obtained based on the difference between the cathodic currents at

199 0.2 V in Ar or O_2 saturated solution. The BOD bioelectrode operational stability was evaluated by

200 chronoamperometry with an applied potential of 0.2 V in air-bubbled PBS (100 mM, pH 7.0).

201 **2.5 Determination of amount of active BOD on the electrodes**

202 The amount of active BOD immobilized on the electrodes was estimated from a standard

203 calibration curve showing a linear relationship between the absorbance change of ABTS and the

204   amount of BOD in solution. In brief, the BOD bioelectrode was carefully washed five times with

205   PBS (100 mM, pH 7.0) and then immersed into air-equilibrated 100 mM PBS (pH 7.0) containing

206   0.50 mg mL^{-1} ABTS with magnetic stirring. After soaking (i.e., 1, 3, 5, 7, 10 min), 500 µL of the

207   reaction solution was withdrawn, and the absorbance measured at 420 nm with an ultraviolet -

208   visible (UV-vis) spectrophotometer (UV-2401PC, SHIMADZU, Japan).(Durand et al., 2012)

209   **2.6 Construction and characterization of gas diffusion bioelectrodes**

210   The BOD bioelectrode was also exploited as a gas diffusion bioelectrode (GDBE) with accelerated

211   gaseous substrate supply. A commercial HCP with one side treated with polytetrafluoroethylene

212   (PTFE) which prevents electrolyte leakage, was used as the gas diffusion support for RGO-A/BOD.

213   The detailed fabrication of the GDBE (surface area: 0.33 cm^2) is described in Supporting

214   Information (SI). The electrochemical characterization was carried out using the three-electrode

215   system in an in-house built electrolyte cell.

216   **2.7 Applications of the GDE in membrane-less glucose/O$_2$ biofuel cells**

217   A GOD bioanode was prepared according to our established procedure (Poon et al., 2018). Briefly,

218   39.2 µL solution, containing 3.3 mg mL^{-1} GOD, 2.0 mg mL^{-1} poly(ethylene glycol)diglycidyl ether

219   (PEGDGE), and 3.2 mg mL^{-1} redox polymer [Os(2,2′-bipyridine)$_2$(polyvinylimidazole)$_{10}$Cl]$^{+/2+}$

220   (Os(bpy)$_2$PVI), was drop-cast onto a nanoporous gold (NPG) electrode. After leaving the electrode

221   in a vacuum desiccator for 20 min, the electrode was transferred into a refrigerator, allowing drying

222   overnight at 4 °C. The GOD bioanode was assembled with the prepared GDBE biocathode and

223   tested in the electrochemical cell containing 12 mL of PBS (100 mM, pH 7.0) with 20 mM glucose.

224   No separating membrane was used due to the high selectivity of BOD and GOD. For the

225   electrochemical characterization of glucose/O$_2$ EBFCs, the bioanode and biocathode were

226   connected to the working and reference/counter electrode, respectively. LSVs with a scan rate of

227   1 mV s^{-1} were recorded to obtain polarization and power density profiles. The power density was

228 normalized to the cathode with a larger geometric surface area of 0.33 cm^2 compared to that of the

229 bioanode.

3. Results and discussion

3.1 Characterization of electrode materials

232 CP consists of 3D-arranged carbon fibers and is suitable as the electrode substrate with high

233 surface area (Chen et al., 2019). As suggested by SEM (Fig. 1a, S3a and S3b), GO is uniformly

234 coated on the fibers. After electrochemical pulse potential treatment in the absence of 4-ABA, the

235 GO nanomaterials coated on CP aggregate because the resulting RGO sheets tend to stack by π–π

236 interactions (Fig. 1c and S3d). Notably, RGO-A shows the mildest aggregation compared to the

237 RGO and RGO-A(N) (Fig. 1b and 1c, and S3c-f). This is most likely due to the presence of –COO$^-$

238 (in neutral solution) on the RGO sheets as introduced by the grafting of 4-ABA (Barbier et al.,

239 1990; Yang et al., 2006). RGO-A with negative charges thus relieves π–π stacking due to

240 electrostatic repulsion between the sheets.

241 For further investigation, GO, RGO and RGO-A were immobilized on highly oriented pyrolytic

242 graphite (HOPG), described in SI, and characterized by AFM with good vertical resolution. It

243 makes good sense that GO (1.2 ± 0.1 nm) is thicker than RGO (0.78 ± 0.03 nm) due to the removal

244 of oxygenated groups *via* electroreduction, Fig. 1d, 1f, S4a-b, S5c-d, S5g-h and Table S1. RGO-

245 A is ~5 Å thicker than RGO (Fig. 1e-f, S4b-c, S5e-f and Table S1), indicative of successful grafting

246 of 4-ABA. Considering the distance (5.63 Å) between the N atom of the NH$_2$ group and the C

247 atom of the COOH group of 4-ABA (Fig. S6) as well as the projected lengths of the C-O and N-

248 H bonds plus van der Waals and hydration lengths, the estimated length of 4-ABA is larger and

249 might be up to 6-7 Å suggesting that the grafted 4-ABA is tilted on the RGO surface.

250 XPS was chosen to map the surface chemical compositions and carbon bonding states of the

251 modified electrodes. The percentages of each carbon species relative to the total amount of carbon

11

252 species, based on the relative surface area of each fitted peak, Fig. 1g-i and S7a-c, with the

253 corresponding binding energies are summarized in Table S2 (Seselj et al., 2018; Tang et al., 2019).

254 The trend of relative surface area of oxygenated carbon species for the electrodes is consistent with

255 the O/C ratio in the survey spectra, indicating satisfactory fitting, Table S2 and Fig. S7d. As noted,

256 the relative amount of oxygenated carbon species including C–O, C=O and COO– increases

257 drastically from 2.3% and 36.7% to 54.8% for bare carbon paper (CP), CP coated with GO (CPG),

258 and CPG with drop-cast GO (CPG/GO), respectively. This variation is caused by the presence of

259 GO with substantial amounts of oxygenated carbon species on the CPG and the increasing amount

260 of immobilized GO on the CPG/GO electrodes.(Tang et al., 2019). After electrochemical potential

261 pulse treatment, the total amount of oxygenated species on the CPG/GO electrodes decreases

262 notably to 18.0%, 14.5% and 8.6% for the RGO, RGO-A and RGO-A(N) electrodes, respectively.

263 This is reasonable because the precursor electrode (*i.e.* CPG/GO) is likely to be electrochemically

264 reduced when a negative potential pulse of -1.4 V is applied, meaning that the GO on the electrode

265 is converted to RGO with much fewer oxygenated groups (Tang et al., 2019). Compared to the

266 RGO electrode with the inevitable C-N impurities (4.4%), larger amounts of C–N species on RGO-

267 A (16.3%) electrodes reflect the successful modification of 4-ABA undergoing electrochemical

268 oxidation at 1.4 V. A small amount of C–N species (5.0%) on RGO-A(N) after the potential pulse

269 of -1.4/0 V due to the presence of physically adsorbed 4-ABA can also be determined. In summary,

270 the observations demonstrate that the electrochemical -1.4/1.4 V potential pulsing can achieve both

271 electroreduction of GO and electro-oxidation of 4-ABA on the CPG/GO electrode in a single step.
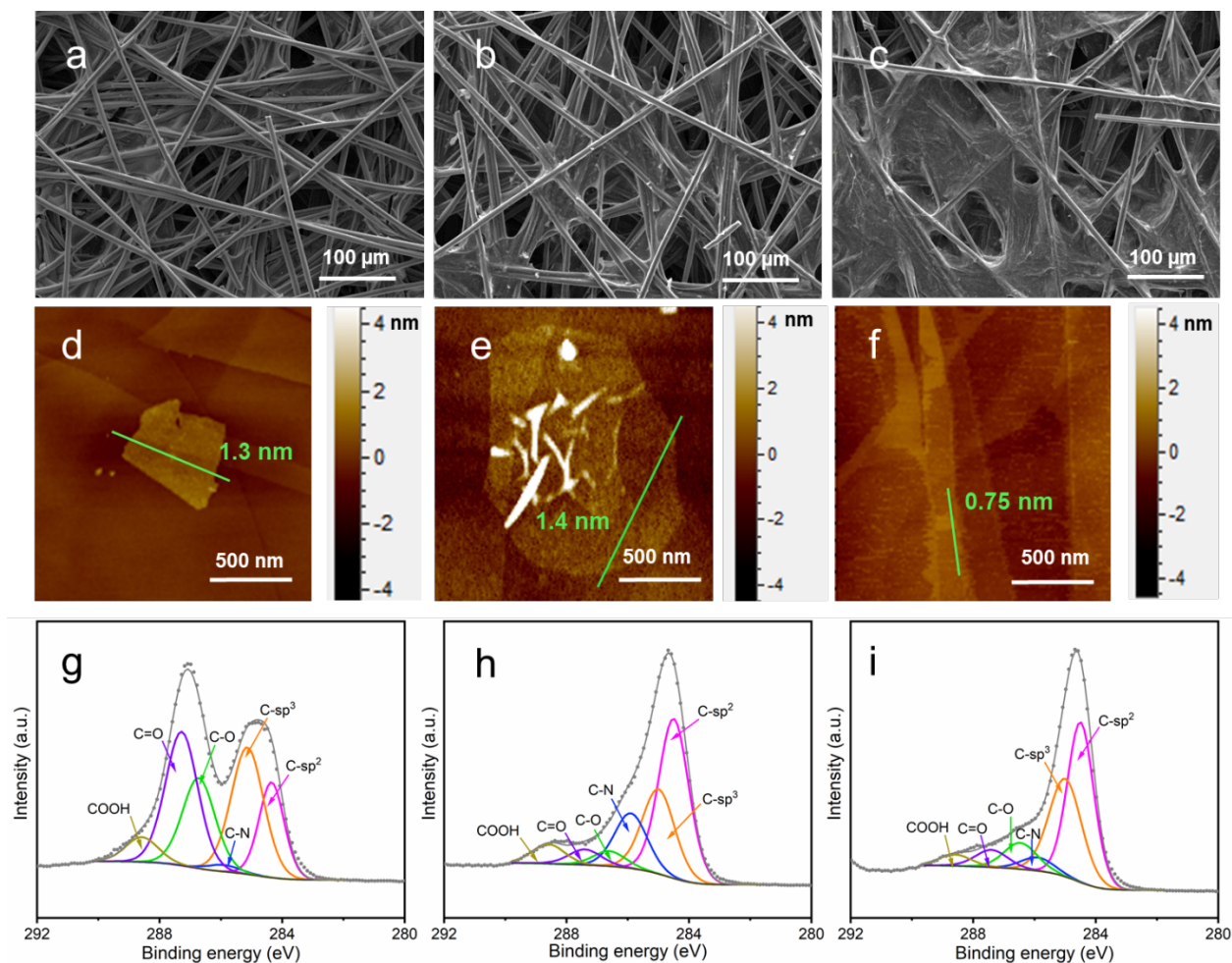
Fig. 1. SEM, AFM images and XPS spectra of (a, d and g) GO, (b, e, and h) RGO-A and (c, f and i) RGO nanomaterials. CP is the substrate for SEM and XPS, while flat HOPG is the support for AFM. The cross-section profiles are shown as Fig. S4.

3.2 Electrochemical characterization of the modified electrodes

Prior to enzyme immobilization, various CP based electrodes were characterized by. EIS in 100 mM PBS (pH 7.0) containing 5.0 mM $K_4[Fe(CN)_6]$ was first carried out. The impedance spectra were fitted using the equivalent circuit in Fig. 2a (Tang et al., 2019). The primary electrode (CPG/GO) gives a moderate charge transfer resistance (R_{ct}) of 50.6 Ω, Table S3. GO-A shows the highest R_{ct} of 341 Ω, in good agreement with the largest peak separation (ΔE_p) of 286 mV and the smallest anodic peak current (0.50 mA cm^{-2}) for the CV of $[Fe(CN)_6]^{3-/4-}$, Fig. 2b and Table S4. The significantly increased R_{ct} and ΔE_p are mainly caused by the stronger electrostatic repulsion

13

284   between the redox probe $[Fe(CN)_6]^{3-/4-}$ and the increased amount of –COOH groups (mostly in –

285   COO^- form at pH 7.0), on the surfaces after electrochemical oxidation of 4-ABA. This is supported

286   by the significantly smaller ΔE_p for positively charged $[Ru(NH_3)_6]^{2+/3+}$. On the other hand,

287   negative potential pulses can reduce GO on the electrode surface and improve the electrode

288   conductivity, supported by R_{ct} decreasing from 50.6 Ω for CPG/GO to 29.0 Ω for the resulting

289   RGO, together with a smaller ΔE_p (from 146 to 105 mV, and from 166 to 107 mV) for both

290    $[Fe(CN)_6]^{3-/4-}$ and $[Ru(NH_3)_6]^{2+/3+}$. When CPG/GO was treated electrochemically with both

291   negative and positive potential pulses, the resulting RGO-A electrode similarly shows a smaller

292   R_{ct} of 32.6 Ω compared to the CPG/GO electrode, consistent with CVs with smaller ΔE_p of 112

293   and 142 mV for $[Fe(CN)_6]^{3-/4-}$ and $[Ru(NH_3)_6]^{2+/3+}$, respectively. In addition, R_{ct} and ΔE_p for

294    $[Fe(CN)_6]^{3-/4-}$ of RGO-A are comparable to those of RGO and RGO-A(N). This is reasonable, as

295   electroreduction of GO greatly enhances the electrochemical activity. Notably, RGO-A(N) shows

296   the smallest ΔE_p (105 mV) for $[Ru(NH_3)_6]^{2+/3+}$ probably due to physically adsorbed 4-ABA

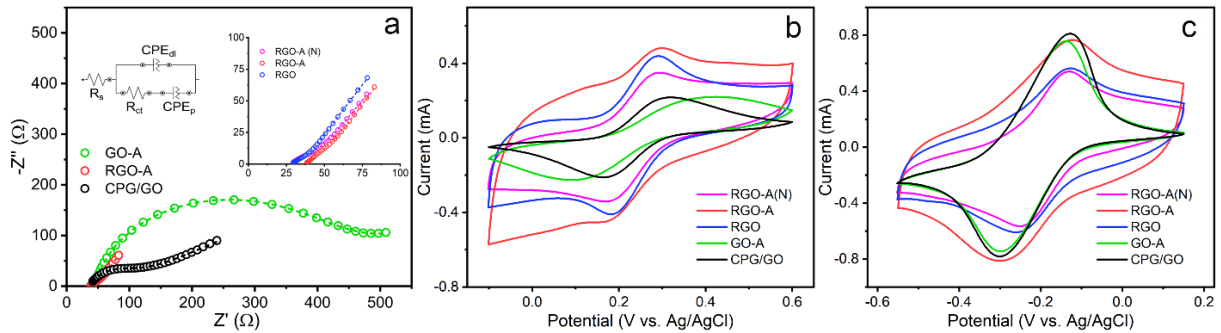297   efficiently attracting the positively charged redox probe molecules.

298
299 **Fig. 2.** (a) EIS of CPG/GO, RGO-A and GO-A electrodes in 100 mM O_2-free PBS (pH 7.0) with
300 5.0 mM $K_4[Fe(CN)_6]$. Inset right in (a): Magnified EIS of RGO-A compared with RGO-A(N) and
301 RGO electrodes. Inset left in (a): Equivalent circuit used for fitting the impedance data. R_s:
302 electrolyte solution resistance. R_{ct}: interfacial electron transfer resistance. CPE_{dl} and CPE_p:
303 constant phase element of the electrode double layer and polarization, respectively. CVs at 50 mV
304 s^{-1} of CPG/GO, GO-A, RGO, RGO-A and RGO-A(N) electrodes in 100 mM O_2-free PBS (pH 7.0)
305 with 5.0 mM (b) $K_4[Fe(CN)_6]$ or (c) $[Ru(NH)_6]Cl_3$.

306   ECSAs of the modified carbon electrodes were estimated roughly from the capacitive currents

307   based on CVs in PBS electrolyte for internal comparison (Tang et al., 2019; Wernert et al., 2018) ,

14

308 Fig. S8 and Table S5. This method is widely used in electrochemistry, since the capacitive current

309 mainly depends on the surface area of the electrode although it could be affected by deviation of

310 the specific capacitance for the modified electrode (Trasatti and Petrii, 1991). Bare CP shows the

311 smallest ECSA of 0.010 ± 0.001 cm^2. CPG shows 50-fold increased ECSA, and CPG/GO nearly

312 further doubles the ECSA of CPG to 1.0 ± 0.2 cm^2 because of the improved hydrophilicity, Fig.

313 S2. Electroreduction of GO to RGO results in a RGO electrode with an ECSA notably increased

314 to 45 ± 8 cm^2 due to the improved conductivity. The RGO-A electrode exhibits the largest ECSA

315 (82 ± 10 cm^2) among the reduced electrodes RGO (45 ± 8 cm^2) and RGO-A(N) (42 ± 4 cm^2),

316 consistent with the SEM observation that the RGO-A electrode shows the mildest RGO sheet

317 aggregation. Overall, the RGO-A electrode with the relatively low R_{ct} and the highest ECSA could

318 be an excellent matrix for BOD immobilization. Both morphology and electrochemical studies

319 thus show that 4-ABA grafting alleviates RGO aggregation by electrostatic repulsion and thus

320 attenuates π–π stacking. After enzyme immobilization, similar trends have been observed, but all

321 ESCAs decrease by about 50% probably due to the presence of insulating protein (Table S5).

322 Overall BOD immobilization and electrocatalytic characterization are therefore accommodated on

323 a set of novel type electrodes which are very well characterized.

3.3 Electrocatalysis of BOD bioelectrodes

325 The ORR on the RGO-A bioelectrodes with BOD immobilized was found to set in at

326 approximately 0.57 V vs. Ag/AgCl (Fig. 3a), consistent with reported observations for other

327 electrode systems (Gutierrez-Sanchez et al., 2016; Xia et al., 2016a). RGO-A/BOD (193 ± 4 µA

328 cm^{-2}) shows 3.4-fold higher Δj_{cat} compared to R-A/BOD (44 ± 5 µA cm^{-2}), Fig. 3a. This can be

329 explained by the more facile electron transfer through the electrode due to the higher RGO content

330 on RGO-A/BOD over R-A/BOD, as disclosed by the increased estimated ECSA from 10 ± 1 cm^2

331 for R-A/BOD to 48 ± 3 cm^2 for RGO-A/BOD (Fig. 3a and Table S5). The loading value of RGO

332   materials governs the "effective" surface area and surface addressability of the modified electrodes.

333   This could be further verified by tuning the amount of drop-cast GO (*i.e.* the amount of resulting

334   RGO) from 1.0 to 3.0 mg mL^{-1} correspondingly reflected in Δj_{cat} of the BOD bioelectrodes, Fig.

335   3b. It is seen that ECSA and Δj_{cat} both increase with increasing concentration of drop-cast GO,

336   until a maximum is reached at 3 mg mL^{-1}. Further increasing concentration of GO solution for

337   electrode modification leads to decreasing Δj_{cat} in spite of a further increased ECSA, Fig. 3b. The

338   decreased catalytic response is probably due to blocked CP network posing diffusion limitation of

339   the substrate O_2 from bulk solution to the electrode surface. This is supported by SEM, which

340   shows that macropores of CP are blocked by highly concentrated RGO aggregation (Fig. S3g). It

341   was, however, clearly confirmed that the dispersed RGO modified 3D bioelectrodes even with

342   lower ECSA showed superior substrate diffusion and catalytic performance than the aggregated

343   RGO modified bioelectrodes.

344   The RGO-A bioelectrode shows a 1.4-fold higher catalytic response compared to the RGO

345   bioelectrode, Fig. 3c, highlighting the role of 4-ABA as a DET promotor grafted on the electrode

346   surface by applying the positive potential pulse (Fig. S9 and S10a). This step is essential for

347   favorable orientation of BOD, since the Cu_{T1} site of *Mv*BOD, surrounded mainly by positive

348   charges at neutral pH (Scheme 1), is then close to the RGO-A electrode surface (Chen et al., 2019).

349   In addition, the RGO-A bioelectrode shows a 2.9-fold higher catalytic response compared to the

350   aggregated RGO-A(N) matrix obtained without positive potential pulse, *i.e.* no chemical grafting

351   of 4-ABA, Fig. S10b. The presence of physically adsorbed 4-ABA on the RGO-A(N) matrix,

352   concluded from XPS (Table S2), could thus still orient BOD to an extent. However, in comparison

353   to RGO-A, RGO-A(N) suffers more serious RGO aggregation, blocking the micropores of 3D CP,

354   and resulting in poorer orientation of BOD for DET as well as slow substrate O_2 diffusion

355   compared with RGO-A. Only 2.6% catalytic activity on the GO-A/BOD bioelectrode compared

356   to RGO-A/BOD, Fig. S10b was observed, highlighting further the importance of electroreduction

357   for improved electrode conductivity. This is supported by the observation that the GO-A/BOD

358   electrode shows only 4.4% ECSA of the RGO-A/BOD electrode, Table S5. Compared to reported

359   BOD behavior on aggregated RGO (size: ca. 200 µm) carbon electrodes with linkers similar to 4-

360   ABA, our RGO-A/BOD bioelectrode showed comparable catalytic performance, but with much

361   smaller amounts of drop-cast enzyme (12.5 vs. 80 µg (Di Bari et al., 2016)). This reflects the

362   superiority of our dispersed RGO-A over aggregated RGO and therefore the very favorable BOD

363   orientation in our RGO-A modified 3D structured electrode in DET-type bioelectrochemistry. It

364   is worth mentioning that the maximum catalytic current density (Δj_{cat}:193 $\pm$ 4 µA cm^{-2}) of our

365   optimized bioelectrodes is obtained in O_2-saturated electrolytes under static conditions, while most

366   reported catalytic responses were obtained from rotating electrodes. The catalytic response

367   obtained in our study is limited by the O_2 diffusion from the bulk solution to the electrode surface.

368   We have prepared a summary table in which the electrocatalytic performance (Δj) of DET-type

369   *Mv*BOD for ORR under static conditions (Table S6) on different surface matrices are compared.

370   Our bioelectrode is seen to show the best competitive performance using the smallest amount of

371   BOD. Different from previous biocathodes as shown in Table S6, CPG/RGO-A is fabricated *via* a

372   facile electrochemical treatment of CPG with RGO and subsequent immobilization of *Mv*BOD.

373   Additionally, CPG/RGO-A can be easily adopted for gas-diffusion electrodes as discussed in
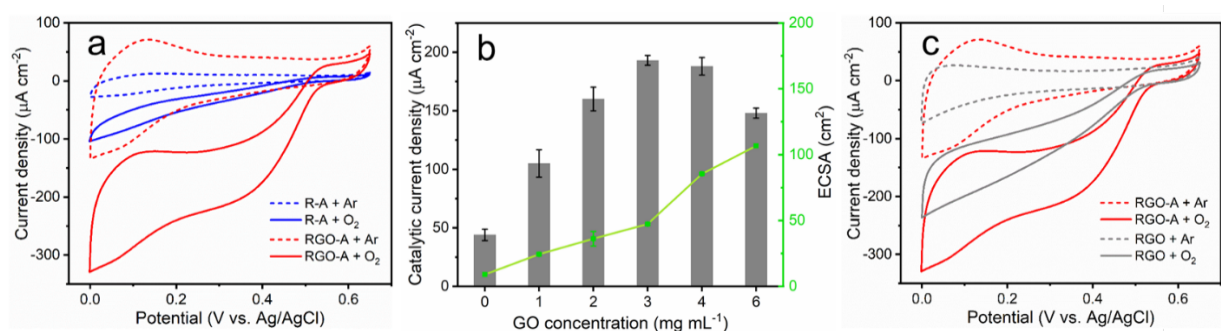
374   Section 3.6.

375

376 **Fig. 3.** CVs of the BOD bioelectrodes based on (a) R-A and RGO-A matrices, as well as (c) RGO-
377 A and RGO matrices in 100 mM PBS (pH 7.0), scan rate 5 mV s^{-1}. (b) Effect of the amount of
378 drop-cast GO (20 µL) on the electrocatalytic performance toward O_2 reduction as well as ECSA
379 of RGO-A/BOD electrodes. All catalytic currents are collected at 0.2 V and background-corrected.

380 **3.4 Kinetic analysis of the bioelectrode performance**

381 We undertook a more detailed kinetic analysis to achieve a better understanding on how 4-ABA

382 functionalization promotes the DET of BOD. The amount of active BOD immobilized on the

383 electrode could, first be estimated by enzyme assay using a spectroscopic method, Fig. S11. The

384 estimated surface coverage, Γ_{act}, of all active BOD in the RGO-A matrix (64 ± 3 pmol cm^{-2}) is

385 comparable to the coverage on the RGO (58.0 ± 0.7 pmol cm^{-2}) and RGO-A(N) matrices (49.3 ±

386 0.7 pmol cm^{-2}), although Δj_{cat} on these three electrode matrices varies somewhat, Table S7. The

387 highest Δj_{cat} on RGO-A is therefore mainly due to higher ratio of BOD able of DET as a result of

388 better enzyme orientation, rather than higher enzyme loading. Further, the catalytic rate constant

389 of immobilized BOD, k_{cat}, is estimated based on the experimental linear sweep voltammetric data

390 for the catalytic current (i) vs. the electrode potential E.

391 Further, to illuminate further the BOD surface binding in the presence and absence of 4-ABA, we

392 treated the data using the model of dispersive catalytic interfacial electron transfer rate constants

393 introduced by Armstrong and associates (Léger et al., 2002) and recently exploited also by Kano

394 and associates (Takahashi et al., 2019; Xia et al., 2016a). Dispersion is incorporated in this model

395 by a uniform distribution of electron transfer distances (d) within a certain range between d_{min} and

396 $d_{min}+\Delta d$, over which electrochemical electron transfer between the electrode and the Cu_{T1} center

397 can occur. Within this range, the standard electrochemical electron transfer rate constant, k_0 is

398 assumed to follow the tunneling form:

$$k_0 = k_0^{max} exp[-\beta(d_{min} + \Delta d)] \tag{1}$$

400   β is the decay factor for tunneling through the intermediate "matter" between the electrode and

401   the Cu_{T1} center ($\approx$ 1-1.4 Å^{-1}). k_0^{max} is a standard rate constant at the lower limit of the distance or

402   orientation distribution ($d = d_{min}$), over which interfacial ET through the protein is feasible. With

403   the presence of the 4-ABA layer, residual tunneling may be inherent also in k_0^{max}.

404   In the model by Armstrong and associates the catalytic current, i is recast as the i/i_{lim}^{cat} vs. E in the

405   two-step form (Léger et al., 2002; Takahashi et al., 2019; Xia et al., 2016a).

406
$$\frac{i}{i_{cat}^{lim}} = \frac{1}{\beta\Delta d\{1+exp(\varphi)\}} \ln \left| \frac{\{1+exp(\varphi)\}+\frac{k_{cat}}{k_0^{max}}exp(\alpha\varphi)}{exp(-\beta\Delta d)\{1+exp(\varphi)\}+\frac{k_{cat}}{k_0^{max}}exp(\alpha\varphi)} \right|$$
(2)

407
$$\varphi = \frac{n_E'F}{RT}(E - E_E^{0'})$$
(3)

408      $i_{cat}^{lim} = (n_S/n_E)\,F \times k_{cat}\lambda\Gamma_{act} \times A$ is the limiting, enzyme controlled current density, where n_S is the

409   number of electrons for the reduction of substrate dioxygen (4), n_E the number of electrons

410   transferred in the enzyme (1), and A the geometric electrode surface area (0.25 cm^2). A (potential

411   independent) enzyme "surface orientation factor", λ (< 1), represents the fraction of the total

412   amount of adsorbed active enzyme capable of DET, so $\Gamma_{DET} = \lambda\Gamma_{act}$. α is the transfer coefficient

413   (0.5), n_E' the number of electrons for interfacial electron transfer between Cu_{T1} and the electrode

414   (1), F the Faraday constant (96485 s A mol^{-1}), R the gas constant (8.314 J·K^{-1}·mol^{-1}), T the absolute

415   temperature (293 K), and $E_E^{0'}$ the formal redox potential of the Cu_{T1} site of BOD that

416   communicates with the electrode by DET (0.473 V vs. Ag/AgCl) (Christenson et al., 2006; Mano

417   and de Poulpiquet, 2018). It is noted that the second step is viewed as a direct single-step

418   intramolecular communication step between the Cu_{T1} center and the substrate reduction at the

419   catalytic Cu_{T2}/Cu_{T3} site.

420   Following previous reports (Takahashi et al., 2019; Xia et al., 2016a), k_{cat}/k_0^{max}, $\beta\Delta d$, and

421      $k_{cat}\lambda\Gamma_{act}$ were used as adjustable parameters to fit Eq. (2) and (3) to the recorded LSV data, Fig. 4a.

422   The catalytic rate constant for DET-capable enzymes, k_{cat}, is different from the solution activity

423   (k_c) due to the different nature of the electron donors. In order to get reasonable fitting, k_{cat}/k_0^{max}

424   is considered as fixed for all the different electrodes. The center of catalytic activity of BOD is

425   thus somewhat remote from the surface and k_{cat} therefore not likely to vary greatly on similar

426   RGO-based electrodes. We shall also take k_0^{max} to be the same for all the ABA-modified

427   electrodes since k_0^{max} largely involves electron transfer (tunneling) across the interface from the

428   carbon surfaces through the bound ABA-unit as well as reorganization free energy terms and other

429   rate parameters that vary little on the protein side. In view of the small structural extension of the

430   bound ABA, tunneling through ABA is only weakly attenuated and may even belong to the

431   adiabatic limit of strong interaction with the electrode surface. With these reservations, the same

432   value of k_0^{max} may be taken also for the electrodes with no bound A. The estimated $k_{cat}\lambda\Gamma_{act}$ for the

433   RGO-A matrix (373 ± 2 pmol cm^{-2} s^{-1}) is higher than for RGO (320 ± 40 pmol cm^{-2} s^{-1}) and RGO-

434   A(N) (156 ± 1 pmol cm^{-2} s^{-1}), in accordance with the trend of Δj_{cat} on these three electrode matrices,

435   Table S7. Furthermore, considering the values for Γ_{act} on the corresponding matrices obtained by

436   the activity assay, and still taking the catalytic activities (k_{cat}) as similar, a larger orientation

437   parameter λ for RGO-A compared to RGO-A(N) is proposed as a main contributor to the improved

438   catalytic performance. However, a comparable λ obtained on RGO-A and RGO would indicate

439   that there is another contributor.

440   $\beta\Delta d$ is evaluated to be smaller than 1 for the RGO-A/BOD electrode, but larger than 8 for the

441   RGO/BOD and 5.0 ± 0.1 for RGO-A(N)/BOD electrodes, Table S7. If β is taken to be 1.0-1.4 Å^{-1}

442   for all the electrodes (Moser et al., 1992), then Δd is formally less than 0.7-1.0 Å for RGO-A/BOD,

443   and in the ranges of 5.7-8.0 Å^{-1} and 3.5-5.1 Å^{-1} for RGO/BOD and RGO-A(N)/BOD, respectively.

444   Δd for RGO-A/BOD is also smaller than the reported value (2.6 ± 0.2 Å) for BOD on a planar

445   electrode (Xia et al., 2016a), indicative of more favorable and narrower BOD orientation

446 distribution on RGO-A electrodes than on all the other electrodes. Taking into account that the

447 BOD size is 4-6 nm (Xia et al., 2016a), most of the DET-capable BOD on the RGO-A matrix

448 would then be in quite narrow orientation distributions. The favorable BOD orientation on the

449 RGO-A matrix is due to the abundance of negatively charged aromatic groups. Based on these

450 kinetic analyses, the promoted DET-type biocatalysis on the RGO-A matrix is thus concluded to

451 be due to the most favorable orientation of BOD (the smallest Δd and largest λ) promoted by the

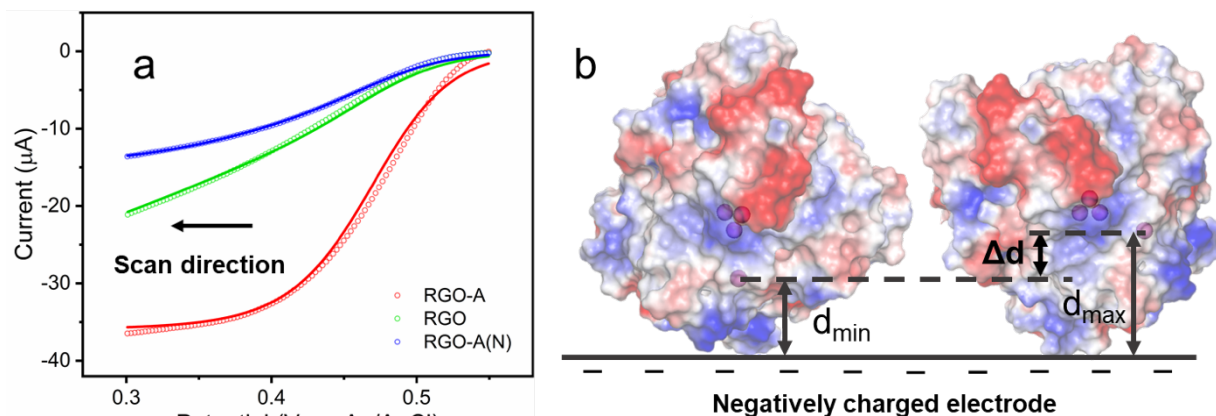452 aromatic 4-ABA groups on the electrode surface.

453
454 **Fig. 4.** (a) Linear sweep voltammograms of catalytic reduction of dioxygen for BOD on RGO-A,
455 RGO or RGO-A(N) matrices at a scan rate of 1 mV s^{-1} in dioxygen-saturated PBS (pH 7.0). The
456 dotted and solid lines represent the raw voltammogram and fitted curves, respectively. (b)
457 Schematic illustration of two boundary orientations of BOD on a negatively charged electrode
458 surface, resulting in different tunneling distances d for interfacial electron transfer from the
459 electrode to the BOD Cu$_{T1}$ site.

3.5 Stability of bioelectrodes

461 We investigated further the storage and operational stability of the BOD bioelectrodes. The RGO-

462 A bioelectrode shows the best storage and operational stability compared to control bioelectrodes,

463 i.e. the RGO bioelectrode and the RGO bioelectrodes with adsorbed 4-ABA (RGO-A(N)), Fig. 5

464 and S12. For example, after two-week storage, the RGO-A bioelectrodes retain 50% of initial

465 catalytic response while the RGO and RGO-A(N) bioelectrodes only retain 25% of the initial value.

466 This highlights the role of 4-ABA in maintaining the electrode stability. Similar to reported

21

467   polycyclic aromatic electrode surface modifiers such as phenylalanine, tyrosine and tryptophan

468   (Blanford et al., 2009), grafted 4-ABA binding to the Cu_{T1} site pocket of the enzyme is proposed

469   further both to stabilize BOD binding and to attenuate conformational changes and therefore

470   denaturation of bound BOD (Gutierrez-Sanchez et al., 2016). Although freshly prepared RGO-

471   A_ads/BOD bioelectrodes, in which BOD is physically adsorbed on the electrode, show a

472   comparable initial electrocatalytic activity and similar kinetic parameters as covalently bound

473   BOD on RGO-A, Table S7, only 35% of the original Δj_{cat} is retained after two weeks' storage.

474   This can be ascribed to BOD leaching from the electrode due to the weak physical interaction, also

475   observed, when BOD is electrostatically adsorbed on glassy carbon (GCE) modified by multi-

476   walled CNTs (MWCNTs) (Al-Lolage et al., 2019).

477   Operational stability of the bioelectrode is another criterion for stability evaluation, which can

478   usually be evaluated by chronoamperometry, chronopotentiometry etc. Here, we use the

479   chronoamperometry technique to evaluate the current density of the BOD bioelectrode

480   continuously in a time course of 60 h, applied with a potential of 0.2 V. Notably, the RGO-A

481   bioelectrode shows superior operational stability with a half-lifetime of 55 h compared to RGO

482   (13 h) and RGO-A_ads/BOD (40 h), Fig. 5b and S12b. The high RGO-A/BOD stability is assigned

483   to the amide bonds between BOD lysine residues and the aromatic 4-ABA carboxylic groups on

484   the graphene-based electrode surface, resulting in minimal leakage and activity loss of BOD

485   (Gutiérrez-Sánchez et al., 2013). Exposed Lys21, Lys181 and Lys408 are proposed to be reactive

486   towards 4-ABA carboxylic groups on the electrode (Singh et al., 2013). Especially, the operational

487   stability of RGO-A bioelectrodes is the best as we can find in the literature for DET-type *Mv*BOD

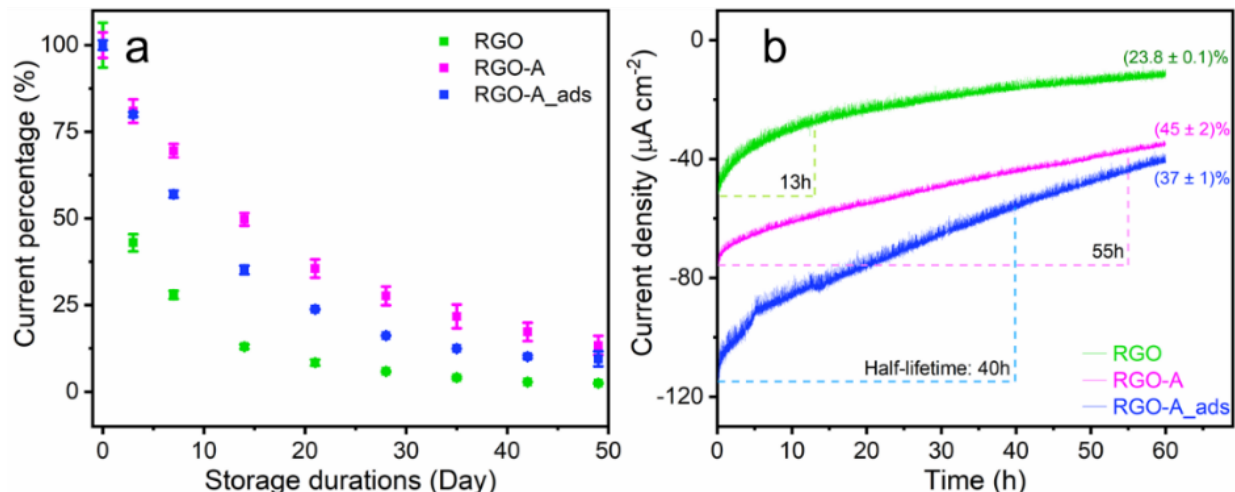488   bioelectrodes under continuous operation (Table 1).

Fig. 5. (a) Storage and (b) operational lifetime of the BOD bioelectrodes on the matrices RGO and RGO-A via covalent bonding, and on RGO-A via physical adsorption (RGO-A_ads) in dioxygen-saturated and air-bubbled PBS (100 mM, pH 7.0). For storage lifetime evaluation, the catalytic activity was recorded by CV on a given day during the storage period. The operational stability of BOD bioelectrodes was evaluated by chronoamperometry with an applied potential of 0.2 V.

Table 1. Comparison of the operational stability of DET-type *Mv*BOD bioelectrodes at given applied potentials for ORR.

Matrix	Immobilization technique	Electrolyte	Operation half-lifetime	Operation conditions	Ref.
CPG/RGO-A	Covalent	PBS, pH 7.0	55 h	0.20 V, air purging	This work
CPG/RGO-A	Adsorption	PBS, pH 7.0	40 h	0.20 V, air purging	This work
Graphite/AuN Ps-MPA	Covalent	Serum-mimic PBS, pH 7.4	~4 h	0.20 V, 500 rpm rotation	(Gutiérrez-Sánchez et al., 2013)
Au/MHA	Covalent	PBS, pH 6.0	~1 h (82%)*	0.20 V, air-saturated	(Gutierrez-Sanchez et al., 2016)
Buckypaper (MWCNTs)	Adsorption	PBS, pH 6.0	10 h	0.50 V, O_2-saturated, stirring	(Walgama et al., 2019)
GCE/MWCN Ts-Cellulose	Adsorption	Citrate buffer, pH 5.0	45 h (60%)*	0.20 V, air purging	(Wu et al., 2009)
Au/CNTs/PA NI	Adsorption	PBS, pH 7.4	12 h (78%)	0.045 V, air-saturated, stirring	(Parunova et al., 2016)

* Retention percentage of initial electrocatalytic activity. AuNPs: Au nanoparticles. MPA: mercaptopropionic acid. MHA: 6-mercaptohexanoic acid. CNTs: carbon nanotubes. PANI: Polyaniline. All potentials are vs. Ag/AgCl (sat.).

3.6 Applications as gas diffusion bioelectrodes and in EBFCs

RGO-A/BOD bioelectrodes have been finally exploited as a GDBE to demonstrate the versatile nature of our bioelectrode construction methodology (Higgins et al., 2011; So et al., 2017). GDBEs are gaining increasing attention as they accelerate the gaseous substrate supply (Chen et al., 2019;

504 Xia et al., 2016b), and possess great potential in portable and wearable EBFCs. GDBEs typically

505 consist of a porous supporting electrode, a gas-diffusion layer, and a biocatalytic layer (So et al.,

506 2017). The consumed gaseous substrate (O_2) for the ORR in the buffer solution can be steadily

507 supplied from the gas phase. CPs are suitable as supporting electrodes. A GDBE cell specialized

508 for membrane-less EBFCs was designed and fabricated (Fig. 6a, 6b, S13 and S14). RGO-A/BOD

509 in an "air-breathing" configuration with gas phase filling of ambient air shows a higher Δj_{cat} of 60

510 μA cm^{-2} working at 0.2 V vs. Ag/AgCl, than the same electrode immersed in the electrolyte (40

511 μA cm^{-2}). The GDBE with enhanced dioxygen supply can thus significantly enhance the

512 electrocatalytic performance, offering considerable potential for practical applications (So et al.,
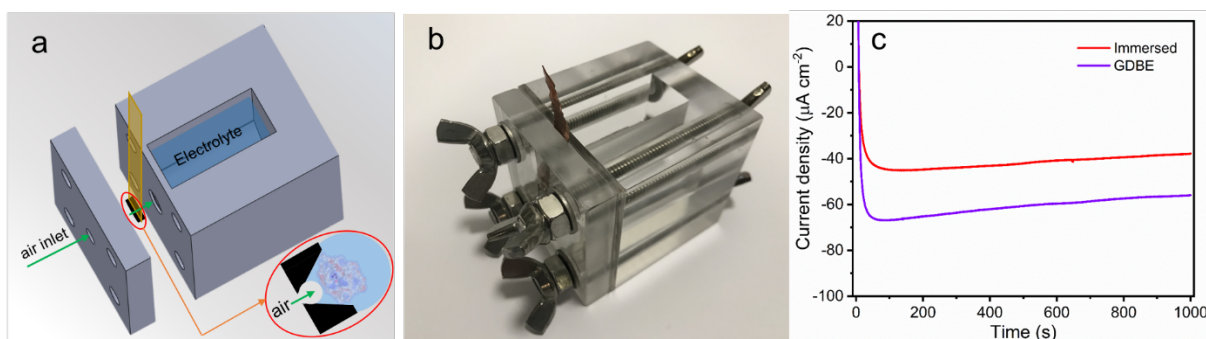
513 2014).

514

515 **Fig. 6.** (a) 3D view and (b) digital photo of the in-house built gas diffusion electrolyte cell. (c)
516 Catalytic performance of the RGO-A/BOD bioelectrode as a GDBE electrode compared to the
517 immersed bioelectrodes, evaluated by chronoamperometry with an applied potential of 0.2 V up
518 to 1000 s.

519 The RGO-A/BOD in GDE configuration was finally assembled with a GOD/Os polymer based

520 bioanode for EBFC applications to demonstrate the feasibility of the BOD biocathode and

521 electricity generation from sugars. The bioanode undergoes mediated electron transfer between

522 GOD and electrode, catalyzing two-electron oxidation of glucose. The constructed glucose/O_2

523 EBFCs delivered a maximum power density (P_{max}) of 22 μW cm^{-2} at 0.22 V, with a short current

524 density of 193 μA cm^{-2} and an open circuit voltage (OCV) of 0.51 V (Fig. 7a), which is comparable

525 to other graphene-based glucose/O_2 EBFCs (Shen et al., 2019a; Tang et al., 2020). The relatively

526 low power density of our constructed glucose/O$_2$ EBFC is due to the limitation by the non-

527 optimized Os polymer/glucose oxidase bioanode, rather than the biocathode. EBFC applications

528 of our RGO-A bioelectrode has in fact demonstrated the feasibility of the BOD biocathode and
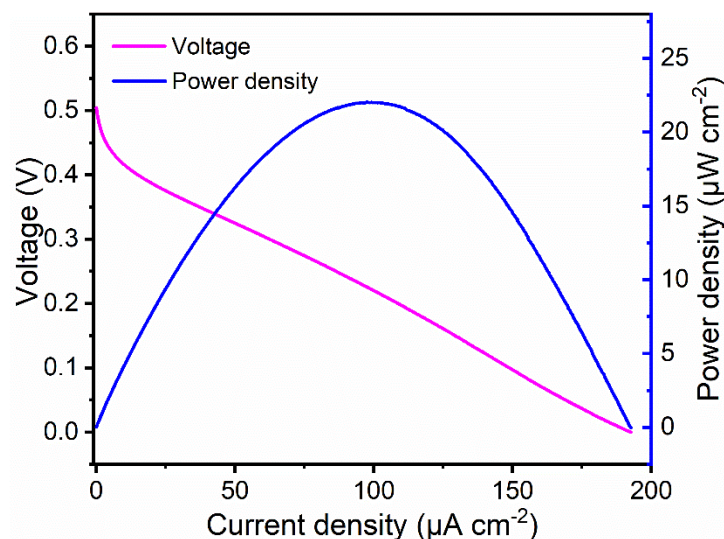
529 electricity generation from sugars.

530

531 **Fig. 7.** Polarization and power density curves obtained from the GOD bioanode and BOD

532 biocathode in air-equilibrated PBS (100 mM, pH 7.0) containing 20 mM glucose.

Conclusions

534 Controlled orientation of electron transfer proteins and redox enzymes on electrochemical surfaces

535 for optimized facile interfacial electrochemical electron transfer is a recurrent challenge. We found

536 that 4-ABA grafting alleviates reduced graphene oxide (RGO) aggregation, a core issue for

537 electrochemical applications of RGO based materials. This new approach represents a universal

538 strategy to retain the high electrochemical surface area and 3D structure of modified carbon paper

539 electrodes, favorable for bioelectrochemical applications. The study offers novel outcomes and

540 perspectives summarized here.

541 A unique and facile electrochemical pulse electrode treatment consisting of cathodic and anodic

542 potential pulses alternatively has been introduced, with the cathodic pulse for graphene oxide

543 reduction and the anodic pulse for 4-ABA grafting. Our single-step electrochemical approach

544 combines in a novel facile synthesis carbon-based surface electrochemistry with robust chemical

545 surface immobilization of 4-ABA. The pulse waveform applied to the electrode has emerged as a

546 facile and promising means of achieving surface modification, in terms of convenience (time and

547 expensive electrochemical equipment) and controllability. However, upscaling of the process

548 might be a challenge by the nonuniform potential distribution of the quite large working electrode.

549 We have furthermore employed a wide range of techniques to map how 4-ABA grafting affects

550 the morphology, thickness and electrochemical properties of modified RGO-based electrodes.

551 Such investigations are rare but the core in the understanding of the interaction between the target

552 enzyme BOD and nanomaterials. Our work offers an intense characterization of modified RGO

553 sheets as supports for the enzyme BOD. This characterization has disclosed an in-depth

554 understanding on how modified nanomaterials enhance the productive interaction between the

555 target enzyme and the nanomaterial-modified electrode, as reflected clearly in the resulting

556 electrochemical performance of the new bioelectrode.

557 The bioelectrocatalytic performance of the bioelectrodes toward dioxygen reduction with the core

558 RGO-A/BOD surface was found to be the most efficient (the highest $\Delta j_{cat} = 193 \pm 4$ µA cm^{-2})

559 among the bioelectrodes prepared and tested. The far superior DET-type biocatalytic performance

560 on the RGO-A matrix over that of the RGO matrix was identified to be caused mainly by more

561 favorable BOD orientation directed by the covalently linked 4-ABA aromatic groups on the

562 electrode surface. This could be supported by the numerical LSV analysis as a useful guide, based

563 on a crude distribution model (Léger et al., 2002; Xia et al., 2016a). Control experiments showed

564 that both negative and positive potential pulses in the surface modification process improve

565 significantly the orientation distribution as represented by the smallest core value of the parameter,

566 $\beta\Delta d$, compared to both the control surfaces and to other reported related carbon based surface types

567 (Takahashi et al., 2019; Xia et al., 2016a). Completive catalytic currents are thus obtained for

568 RGO-A/BOD electrodes as for reported *Mv*BOD electrodes, but with much smaller amounts of

569 drop-cast enzymes (Di Bari et al., 2016).

570 As a final major observation of our study, a merit of the new RGO-A/BOD bioelectrode is the

571 operational stability. With a half-lifetime stability of 55 h the RGO-A/BOD bioelectrode stability

572 also exceeds the stability of all previously reported *Mv*BOD electrode systems. This would be a

573 particular merit in practical use such as in EBFCs. The high rate of interfacial electron transfer

574 between BOD and the 3D matrix and the high stability of the RGO-A/BOD bioelectrode are likely

575 ascribed to alleviation of the RGO aggregation due to the electrostatic repulsion among the 4-

576 ABA-functionalized RGO sheets and a retention of a high surface area. The dual roles of grafting

577 of 4-ABA, at the same time as a bioelectrochemical electron transfer promotor and as an efficient

578 enzyme stabilizer are thus highlighted by the results of our study.

579 In summary, the alleviation of RGO aggregation is important and the methodologies, especially

580 the grafting of functional groups for alleviated RGO aggregation, and the strong stabilization of

581 the integrated functional RGO-A/BOD unit proposed in this work can most likely be extended to

582 other electrochemical RGO and carbon-based applications, in this way opening new entrance for

583 pure and applied bioelectrochemistry.

584

585 **Declaration of competing interest**

586 There are no conflicts to declare.

587

588 **Acknowledgements**

597 **Appendix A. Supplementary data**

598 Supplementary data to this article can be found online at xxx.
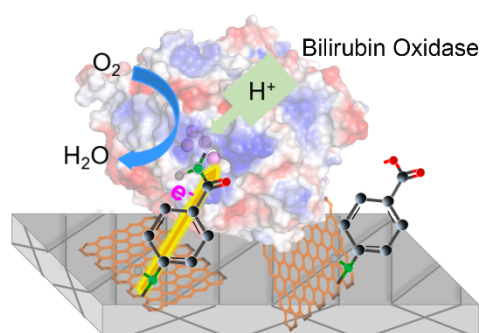
599 **References**

600 Al-Lolage, F.A., Bartlett, P.N., Gounel, S., Staigre, P., Mano, N., 2019. ACS Catal. 9(3), 2068-2078.

601 Barbier, B., Pinson, J., Desarmot, G., Sanchez, M., 1990. J. Electrochem. Soc. 137(6), 1757-1764.

602 Blanford, C.F., Foster, C.E., Heath, R.S., Armstrong, F.A., 2009. Faraday Discussions 140(0), 319-335.

603 Chen, X., Yin, L., Lv, J., Gross, A.J., Le, M., Gutierrez, N.G., Li, Y., Jeerapan, I., Giroud, F., Berezovska, A.,
604 O'Reilly, R.K., Xu, S., Cosnier, S., Wang, J., 2019. Adv. Funct. Mater. 29(46), 1905785.

605 Chi, Q., Farver, O., Ulstrup, J., 2005. PANS 102(45), 16203-16208.

606 Christenson, A., Shleev, S., Mano, N., Heller, A., Gorton, L., 2006. BBA-Bioenergetics 1757(12), 1634-1641.

607 Cracknell, J.A., McNamara, T.P., Lowe, E.D., Blanford, C.F., 2011. Dalton Trans. 40(25), 6668-6675.

608 Di Bari, C., Goñi-Urtiaga, A., Pita, M., Shleev, S., Toscano, M.D., Sainz, R., De Lacey, A.L., 2016. Electrochim.
609 Acta 191, 500-509.

610 Dreyer, D.R., Park, S., Bielawski, C.W., Ruoff, R.S., 2010. Chem. Soc. Rev. 39(1), 228-240.

611 Durand, F., Kjaergaard, C.H., Suraniti, E., Gounel, S., Hadt, R.G., Solomon, E.I., Mano, N., 2012. Biosens.
612 Bioelectron. 35(1), 140-146.

613 Gray, H.B., Winkler, J.R., 2010. BBA-Bioenergetics 1797(9), 1563-1572.

614 Gross, A.J., Chen, X., Giroud, F., Travelet, C., Borsali, R., Cosnier, S., 2017. J. Am. Chem. Soc. 139(45), 16076-
615 16079.

616 Gutierrez-Sanchez, C., Ciaccafava, A., Blanchard, P.Y., Monsalve, K., Giudici-Orticoni, M.T., Lecomte, S.,
617 Lojou, E., 2016. ACS Catal. 6(8), 5482-5492.

618 Gutiérrez-Sánchez, C., Pita, M., Toscano, M.D., De Lacey, A.L., 2013. Electroanalysis 25(6), 1359-1362.

619 Hernández-Cancel, G., Suazo-Dávila, D., Ojeda-Cruzado, A.J., García-Torres, D., Cabrera, C.R., Griebenow,
620 K., 2015. J. Nanobiotechnol. 13(1), 70.

621 Higgins, S.R., Lau, C., Atanassov, P., Minteer, S.D., Cooney, M.J., 2011. ACS Catal. 1(9), 994-997.

622 Korani, A., Salimi, A., 2015. Electrochim. Acta 185, 90-100.

623 Lalaoui, N., Le Goff, A., Holzinger, M., Cosnier, S., 2015. Chem. Eur. J. 21(47), 16868-16873.

624 Lawal, A.T., 2019. Biosens. Bioelectron. 141, 111384.

625   Le, T.X.H., Bechelany, M., Engel, A.B., Cretin, M., Tingry, S., 2016. Electrochim. Acta 219, 121-129.

626   Léger, C., Jones, A.K., Albracht, S.P.J., Armstrong, F.A., 2002. J. Phys. Chem. B 106(50), 13058-13063.

627   Li, X., Li, D., Zhang, Y., Lv, P., Feng, Q., Wei, Q., 2020. Nano Energy 68, 104308.

628   Li, X., Xu, Y., Hu, G., Luo, Z., Xu, D., Tang, T., Wen, J., Li, M., Zhou, T., Cheng, Y., 2018. Electrochim. Acta
629   280, 33-40.

630   Lopez, R.J., Babanova, S., Ulyanova, Y., Singhal, S., Atanassov, P., 2014. ChemElectroChem 1(1), 241-248.

631   Mano, N., de Poulpiquet, A., 2018. Chem. Rev. 118(5), 2392-2468.

632   Mazurenko, I., Monsalve, K., Rouhana, J., Parent, P., Laffon, C., Goff, A.L., Szunerits, S., Boukherroub, R.,
633   Giudici-Orticoni, M.-T., Mano, N., Lojou, E., 2016. ACS Appl. Mater. Inter. 8(35), 23074-23085.

634   Moser, C.C., Keske, J.M., Warncke, K., Farid, R.S., Dutton, P.L., 1992. Nature 355(6363), 796-802.

635   Murata, K., Kajiya, K., Nakamura, N., Ohno, H., 2009. Energy Environ. Sci. 2(12), 1280-1285.

636   Olejnik, P., Palys, B., Kowalczyk, A., Nowicka, A.M., 2012. J. Phys. Chem. C 116(49), 25911-25918.

637   Parunova, Y.M., Bushnev, S.O., Gonzalez-Arribas, E., Falkman, P., Lipkin, A.V., Popov, V.O., Shleev, S.V.,
638   Pankratov, D.V., 2016. Russian J. Electrochem. 52(12), 1166-1171.

639   Pavlidis, I.V., Patila, M., Bornscheuer, U.T., Gournis, D., Stamatis, H., 2014. Trends Biotechnol. 32(6), 312-
640   320.

641   Poon, K.C., Ma, X., Tan, D.C.L., Su, H., Sato, H., 2018. ACS Catal. 8(6), 4950-4954.

642   Qiu, H.-J., Guan, Y., Luo, P., Wang, Y., 2017. Biosens. Bioelectron. 89, 85-95.

643   Ruff, A., Szczesny, J., Marković, N., Conzuelo, F., Zacarias, S., Pereira, I.A.C., Lubitz, W., Schuhmann, W.,
644   2018. Nat. Commun. 9(1), 3675.

645   Samejima, T., Wu, C.-S.C., Shiboya, K., Kaji, H., Koikeda, S., Ando, K., Yang, J.T., 1994. J. Protein Chem. 13(3),
646   307-313.

647   Seselj, N., Engelbrekt, C., Ding, Y., Hjuler, H.A., Ulstrup, J., Zhang, J., 2018. Adv. Energy Mater. 8(13),
648   1702609.

649   Shen, F., Pankratov, D., Halder, A., Xiao, X., Toscano, M.D., Zhang, J., Ulstrup, J., Gorton, L., Chi, Q., 2019a.
650   Nanoscale Adv. 1(7), 2562-2570.

651   Shen, F., Pankratov, D., Pankratova, G., Toscano, M.D., Zhang, J., Ulstrup, J., Chi, Q., Gorton, L., 2019b.
652   Bioelectrochemistry 128, 94-99.

653   Siepenkoetter, T., Salaj-Kosla, U., Xiao, X., Belochapkine, S., Magner, E., 2016. Electroanalysis 28(10), 2415-
654   2423.

655   Siepenkoetter, T., Salaj-Kosla, U., Xiao, X., Conghaile, P.Ó., Pita, M., Ludwig, R., Magner, E., 2017.
656   ChemPlusChem 82(4), 553-560.

657   Singh, K., McArdle, T., Sullivan, P.R., Blanford, C.F., 2013. Energy Environ. Sci. 6(8), 2460-2464.

658   So, K., Kawai, S., Hamano, Y., Kitazumi, Y., Shirai, O., Hibi, M., Ogawa, J., Kano, K., 2014. Phys. Chem.Chem.
659   Phys. 16(10), 4823-4829.

660   So, K., Sakai, K., Kano, K., 2017. Curr. Opin. Electrochem. 5(1), 173-182.

661   Takahashi, Y., Wanibuchi, M., Kitazumi, Y., Shirai, O., Kano, K., 2019. J. Electroanal. Chem. 843, 47-53.

662   Tang, J., Werchmeister, R.M.L., Preda, L., Huang, W., Zheng, Z., Leimkühler, S., Wollenberger, U., Xiao, X.,
663   Engelbrekt, C., Ulstrup, J., Zhang, J., 2019. ACS Catal. 9(7), 6543-6554.

664   Tang, J., Yan, X., Engelbrekt, C., Ulstrup, J., Magner, E., Xiao, X., Zhang, J., 2020. Bioelectrochemistry 134,
665   107537.

666   Trasatti, S., Petrii, O.A., 1991. Pure Appl. Chem. 63(5), 711.

667   Walgama, C., Pathiranage, A., Akinwale, M., Montealegre, R., Niroula, J., Echeverria, E., McIlroy, D.N.,
668   Harriman, T.A., Lucca, D.A., Krishnan, S., 2019. ACS Appl. Bio. Mater. 2(5), 2229-2236.

669 Wang, F.-T., Wang, Y.-H., Xu, J., Huang, K.-J., Liu, Z.-h., Lu, Y.-f., Wang, S.-y., Han, Z.-w., 2020. Nano Energy
670 68, 104310.

671 Wei, S., Hao, Y., Ying, Z., Xu, C., Wei, Q., Xue, S., Cheng, H.-M., Ren, W., Ma, L.-P., Zeng, Y., 2020. J. Mater.Sci.
672 Technol. 37, 71-76.

673 Werchmeister, R.M.L., Tang, J., Xiao, X., Wollenberger, U., Hjuler, H.A., Ulstrup, J., Zhang, J., 2019. J.
674 Electrochem. Soc. 166(16), G170-G177.

675 Wernert, V., Lebouin, C., Benoit, V., Gadiou, R., de Poulpiquet, A., Lojou, E., Denoyel, R., 2018. Electrochim.
676 Acta 283, 88-96.

677 Wu, X., Zhao, F., Varcoe, J.R., Thumser, A.E., Avignone-Rossa, C., Slade, R.C.T., 2009. Biosens. Bioelectron.
678 25(2), 326-331.

679 Xia, H.-q., Kitazumi, Y., Shirai, O., Kano, K., 2016a. J. Electroanal. Chem. 763, 104-109.

680 Xia, H.-q., So, K., Kitazumi, Y., Shirai, O., Nishikawa, K., Higuchi, Y., Kano, K., 2016b. J. Power Sources 335,
681 105-112.

682 Xiao, X., Conghaile, P.Ó., Leech, D., Ludwig, R., Magner, E., 2017. Biosens. Bioelectron. 90, 96-102.

683 Xiao, X., McGourty, K.D., Magner, E., 2020. J. Am. Chem. Soc. 142(26), 11602-11609.

684 Xiao, X., Siepenkoetter, T., Conghaile, P.Ó., Leech, D., Magner, E., 2018. ACS Appl. Mater. Inter. 10(8),
685 7107-7116.

686 Xiao, X., Xia, H.-q., Wu, R., Bai, L., Yan, L., Magner, E., Cosnier, S., Lojou, E., Zhu, Z., Liu, A., 2019. Chem.
687 Rev. 119, 9509-9558.

688 Yang, G., Shen, Y., Wang, M., Chen, H., Liu, B., Dong, S., 2006. Talanta 68(3), 741-747.

689 Yang, K., Chen, B., Zhu, L., 2015. Sci. Rep. 5(1), 11641.

690 Yu, Y., Nyein, H.Y.Y., Gao, W., Javey, A., 2019. Adv. Mater., 1902083.

691 Zhao, C.-e., Gai, P., Song, R., Chen, Y., Zhang, J., Zhu, J.-J., 2017. Chem. Soc. Rev. 46(5), 1545-1564.

692 Zhao, G., Jiang, L., He, Y., Li, J., Dong, H., Wang, X., Hu, W., 2011. Adv. Mater. 23(34), 3959-3963.
693
694

695 **Graphic TOC**:

696
697